Synthesis and characterization of quaternary PtRuIrSn/C electrocatalysts for direct ethanol fuel cells

K. Fatih*, V. Neburchilov, V. Alzate, R. Neagu, H. Wang

National Research Council Canada, Institute for Fuel Cell Innovation, 4250 Westbrook Mall, Vancouver, British Columbia V6T 1W5, Canada

ARTICLE INFO

ABSTRACT

To find a more durable anode with high performance for direct ethanol fuel cells (DEFCs), the present study investigates a series of quaternary electrocatalysts, $Pt_{30}Ru_{30}Ir_{40-x}Sn_x/C$ (wt.%), for the ethanol electro-oxidation reaction (EOR). The carbon-supported $Pt_{30}Ru_{30}Ir_{40-x}Sn_x/C$ electrocatalysts were prepared by a known impregnation-reduction (borohydride) method. The microstructure and chemical composition were determined by X-ray diffraction (XRD), energy dispersive X-ray spectroscopy (EDX) and transmission electron microscopy (TEM). The activity of the electrocatalysts for EOR was compared to commercial $Pt_{67}Ru_{33}/C$ (HISPEC5000) using linear sweep voltammetry (LSV) based on similar Pt loading. The results of this study show that electrocatalyst composition with 10 and 20% Ir (wt.%) exhibit higher electrocatalytic activity than the commercial PtRu electrocatalyst. The single fuel cell testing at 90 °C comparing $Pt_{30}Ru_{30}Ir_{40-x}Sn_x/C$ to commercial $Pt_{67}Ru_{33}/C$ and $Pt_{83}Sn_{17}/C$ anodes showed an enhancement of Pt activity (normalized to Pt loading) in the following order: $Pt_{30}Ru_{30}Ir_{10}Sn_{30} > Pt_{30}Ru_{30}Sn_{40} \geq Pt_{30}Ru_{30}Ir_{40} \geq Pt_{83}Sn_{17} > Pt_{67}Ru_{33}$. After a long-term performance test, the activity changed to the following order: $Pt_{30}Ru_{30}Ir_{10}Sn_{30} > Pt_{30}Ru_{30}Ir_{40} > Pt_{30}Ru_{30}Sn_{40} > Pt_{83}Sn_{17} > Pt_{67}Ru_{33}$. $Pt_{30}Ru_{30}Ir_{10}Sn_{30}/C$ exhibited both a higher performance with a specific power density of 29 mW mg$_{Pt}^{-1}$ without O_2 backpressure at the cathode and an excellent long-term stability in a DEFC operating at 90 °C.

Crown Copyright © 2010 Published by Elsevier B.V. All rights reserved.
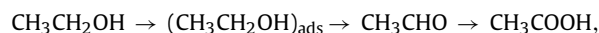
1. Introduction

Direct ethanol fuel cells (DEFCs) are a promising fuel cell technology that has the potential to reach similar performance levels as direct methanol fuel cells. Furthermore, ethanol is relatively safer than methanol and has a higher theoretical mass energy than methanol (8 kWh kg^{-1} vs. 6.1 kWh kg^{-1}) [1]. The mechanism of a complete ethanol electro-oxidation reaction (EOR) involves 12 electrons and the breaking of a C–C bond, in contrast to methanol electro-oxidation, which involves only six electrons and no C–C bond breaking on a similar type of anode material. The application of DEFC requires the breaking of a C–C bond when energy efficiency is required. However, for some small scale applications, such as powering electronic devices or when using DEFC as a sensor such as in breathalyzers, the cell durability and reliability are the main requirements. Ethanol oxidation in acid media occurs with the adsorption of acetyl species and the formation of stable intermediate products such as acetaldehyde and acetic acid [2–5]. Shown below are parallel reactions proposed for ethanol oxidation [4]:

Total-oxidation :

$$CH_3CH_2OH \rightarrow (CH_3CH_2OH)_{ads} \rightarrow C1_{ad}, C2_{ad} \rightarrow CO_2$$

Partial-oxidation :

$$CH_3CH_2OH \rightarrow (CH_3CH_2OH)_{ads} \rightarrow CH_3CHO \rightarrow CH_3COOH,$$

where $C1_{ad}$ and $C2_{ad}$ represent adsorbed intermediates with one and two carbon atoms, respectively.

The common anodes in DEFC are based on PtSn and PtRu catalysts in which the adsorption and decomposition of ethanol occurs on Pt sites and dissociative adsorption of water occurs on the Sn or Ru sites. During the dissociative adsorption of ethanol on Pt sites, Sn or Ru supplies the O-species for the oxidation of CO-like species [2,6–12]. Jiang et al. [6] established a correlation between the structures of PtSn alloy and Pt–SnO$_2$, prepared by the polyol method, which respectively inhibit and allowing the hydrogen adsorption/desorption process. It was deduced that SnO$_2$ in the vicinity of Pt has the ability to promote the oxidation of CO-like species resulting from ethanol oxidation. Antolini et al. [13] explained the positive effect of Ru addition on the catalytic activity of PtSn/C prepared by chemical reduction with formic acid, using the ratio of

* Corresponding author. Tel.: +1 604 221 3071; fax: +1 604 221 3001.
E-mail address: Khalid.Fatih@nrc.gc.ca (K. Fatih).

components PtSnRu (1:1:0.3) at 40 and 90 °C, by the interactions between Sn and Ru oxides. However, the effect of the addition of Ru was not always positive; the ratio of PtSnRu (1:1:1) showed a lower activity than the binary catalysts PtSn/C and PtRu/C. Contrasting results were obtained with the anode PtRuSn/C (1:1:1) produced by the polyol method, which showed an improved performance in DEFC in comparison with PtRu/C (1:1) but lower performance than PtSn/C (1:1) [14]. The developed catalyst had a shorter lattice parameter than PtSn/C (1:1) and a longer one than Pt/C and PtRu/C (1:1). Another active ternary composition, PtSnRu/C (86:10:4), also demonstrated an enhanced performance relative to Pt–Sn/C (90:10) in a single-cell DEFC [15]. In this study, the drop in the performance of PtSnRu/C (86:10:4) and PtSn/C (90:10) was attributed to the formation of non-catalytic and less conductive tin oxides. The difference in the performance results of PtSnRu/C [13–15] could be explained mainly by the difference in the methods employed for the preparation of the catalysts. For example, with binary catalysts, Lamy's group obtained the optimum performance with Pt:Sn (9:1) using methods such as co-impregnation-reduction [16] and the Bönneman method [17]. Conversely, Xin's group found that optimum performances were obtained with higher Sn content (PtSn (2:1) to PtSn (1:1)) using a modified-polyol method [18]. In most of these studies, Sn was found in a non-alloyed oxidized form according to XRD patterns.

It is known that along with Ru and Sn, Ir also activates and promotes the electro-oxidation of adsorbed CO-like species, as seen in DEFC [19] and DMFC [20,21]. de Tacconi et al. [22] investigated ethanol oxidation on Ir and Rh electrodes by the FTIR method, and they found that electro-oxidation of ethanol on Ir is selective and produces mainly acetic acid, while on Rh it produces CO_2. Cao et al. [19] showed a higher rate of EOR on Ir_3Sn/C than on Pt/C and Pt_3Sn/C in a low potential range at 90 °C in a DEFC. IrO_2 and RuO_2 were used as modifiers for the activation of ethanol on Pt [23]. The addition of IrO_2 to Pt–RuO_2 shifts ethanol oxidation to lower potentials. Chen et al. [24] used IrO_2 to increase the methanol oxidation rate on $PtIrO_2$/C. The IrRu carbon supported/unsupported (88%Ir12%Ru)/C anodes showed higher performance than PtRu/C in DMFC [25]. The known high durability of Ir and IrO_2 in regenerative fuel cells for the oxygen reduction reaction (ORR) and the oxygen evolution reaction (OER) was used to stabilize the PtSn/C in acid solutions in DEFC [26,27]. Ribeiro et al. [28] developed the ternary composition 40% (PtSnIr)/C on carbon Vulcan XC-72 with particle sizes of 2–8 nm prepared by thermal decomposition of polymeric precursors method. This composition showed higher power density, when normalized with respect to the Pt loading, compared to binary compositions of 40% (PtSn)/C and 40% (PtIr)/C. It was also shown that the compositions 40% ($Pt_{68}Sn_9Ir_{23}$)/C and 40% ($Pt_{89}Sn_{11}$)/C have a higher durability and activity, respectively, for ethanol oxidation.

The aim of the present work is to investigate and report on the development of quaternary PtRuIrSn/C catalysts and their activity and long-term stability toward ethanol electro-oxidation in a DEFC. The development of these catalysts is based on the promoting effect of Sn and Ru in the low and high potential regions, respectively, combined with the stabilizing and promoting effect of Ir. To reduce the Pt content, the approach used in this study consisted of replac-ing some of the 60 wt.% of Pt in the base material $Pt_{67}Ru_{33}$/C (wt.%) with Ir followed by a gradual substitution of Ir with Sn in the quaternary composition $Pt_{30}Ru_{30}Ir_{40-x}Sn_x$/C (wt.%). The performance was compared to commercial $Pt_{67}Ru_{33}$/C (wt.%).

2. Experimental

2.1. Preparation of electrocatalysts

A series of carbon-supported catalysts, $Pt_{30}Ru_{30}Ir_{40-x}Sn_x$/C (wt.%), with a fixed total metal loading on carbon of 30 wt.% were prepared by the known borohydride chemical reduction method. The carbon black Vulcan XC-72 was dispersed in hot distilled water (80 °C), treated with an ultrasonic probe for 30 min and stirred overnight. All of the noble metal compounds $PtCl_4$, $H_2IrCl_6 \cdot H_2O$, $SnCl_2 \cdot 2H_2O$ and $RuCl_3 \cdot H_2O$ (all from Aldrich) were dissolved in 3 M HCl. The carbon suspension was then added to the mixed solutions of metals and heated to 80 °C for 1 h. After, the final solution was treated with an ultrasonic probe for 1 h and stirred overnight. The pH of the final solution was adjusted to pH 10 with NaOH (10N). The reduction of metal ions to metal was carried out by slow addition (drop wise) of the reducing agent, 5% $NaBH_4$ (40 molar excess [29,30]) at $T = 80$ °C [31] over 3 h. After the complete addition of the reducing agent, the solution was stirred overnight at room temperature. The decantation of the final solution was performed in a centrifuge at 3000 rpm and was followed by washings until a neutral pH was achieved. The catalyst powders were dried at 100 °C and ground for 2 min in a high power grinder (IKA). All prepared catalysts were sintered at 400 °C for 1 h under a nitrogen atmosphere.

2.2. Physicochemical characterization

The compositions of the prepared anodes are given in Table 1. Quantitative analysis was done by EDX (Oxford Instruments Link Pentafet coupled with a Hitachi S3500N SEM). For simplicity, all catalysts will be presented based on their nominal weight percentage composition (wt.%). The catalyst surface area was determined by BET using a Couler SA3100 analyzer. XRD analysis was performed on the diffractometer, Brüker D8 Advance, with a Cu Kα radiation source and a Goebel mirror for parallel incident beam. LaB_6 standard was used as a reference to correct for instrument contribution to the width of the diffraction peaks. Microstructural investigations and evaluation of particles' size were done on transmission electron microscope (TEM) images acquired using Hitachi H7600 LaB_6 and FEI Tecnai G2 FEG TEMs. The TEM samples were prepared by dispersing the catalyst powder on carbon-coated 300 mesh grids.

2.3. Electrochemical characterization

Electrodes for electrochemical testing were prepared by depositing a known amount of catalyst-containing ink on graphite rods (diameter 5 mm, Alfa Aesar) followed by Nafion impregnation (3 μl of Nafion 0.05 wt.% in ethanol). The ink was prepared by dispersion of the catalyst powders in pure ethanol. The Pt loading of the catalyst coating was 27 μg cm^{-2} in all cases. The electrodes were tested in a three-electrode glass cell. The ohmic

Table 1
EDX composition of $Pt_{30}Ru_{30}Ir_{40-x}Sn_x$/C prepared by borohydride reduction method and commercial $Pt_{67}Ru_{33}$/C (Johnson Matthey Inc.).

Electrocatalyst	Nominal composition (wt.%)	Nominal composition (at.%)	EDX (wt.%)	EDX (at.%)
PtRuIrSn/C	30:30:40:0	23:45:32:0	24:33:43:0	18:49:33:0
	30:30:30:10	22:43:23:12	29:27:33:11	22:39:25:14
	30:30:20:20	21:41:14:23	26:20:32:22	19:29:25:27
	30:30:10:30	20:39:7:34	29:22:14:35	20:30:10:40
	30:30:0:40	20:38:0:43	37:16:0:47	26:21:0:53
PtRu/C	67:33	50:50	64:36	48:52
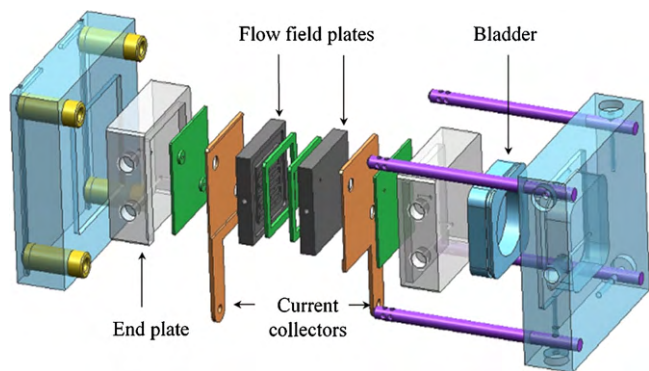
Fig. 1. Expanded view of a direct ethanol fuel cell hardware.

Fig. 2. XRD patterns of nominal compositions $Pt_{30}Ru_{30}Ir_{40-x}Sn_x/C$ with $0 < x < 40$ (wt.%) prepared by borohydride reduction method on Vulcan XC-72 (30 wt.% metal loading). (□) Carbon support and (*) SnO_2 phase.

drop was not specifically taken into account for this work. The electrochemical measurements were carried out with a Solartron 1480 multi-channel electrochemical station. An $Hg/Hg_2SO_4/0.5$ M H_2SO_4 reference electrode was used to avoid any chloride contamination, and the potentials were later converted to potentials against a standard hydrogen electrode (SHE). The electrolyte 0.5 M H_2SO_4 was de-aerated by bubbling pure N_2 for 30 min followed by a CV cycling (10 cycles) at 100 mV s^{-1} between 0 and 0.6 V (SHE). Immediately after CV cycling, ethanol was added to make a 1 M EtOH + 0.5 M H_2SO_4 solution, and the anode potential was held at 50 mV for 30 min while bubbling with N_2. Commercial PtRu catalyst from JM (HISPEC5000) was used as a reference. LSV curves were measured in the working DEFC potential range 0–0.6 V (SHE) at a scan rate of 1 mV s^{-1} and 20 °C. All measurements were repeated at least three times for reproducibility.

2.4. DEFC single-cell characterization

DEFC cell performance testing was conducted in a custom-built 5 cm^2 single fuel cell. An expanded view of the cell is shown in Fig. 1. The membrane electrode assembly (MEA) was fabricated by sandwiching a Nafion® membrane N117 between two gas diffusion electrodes (GDE) [32]. The Nafion® N117 membrane was pre-treated for 30 min in a 3 wt.% H_2O_2 solution at 90 °C, boiled in 0.5 M H_2SO_4 for 30 min then rinsed and stored in de-ionized (DI) water. GDEs were prepared by spraying the catalyst ink onto a carbon fiber paper (CFP) (Toray TGP-H-120). Wet-proofed (10 wt.% poly(tetrafluoroethylene), PTFE) and non wet-proofed CFP were used for the cathode and the anode, respectively. The catalyst ink consisted of a mixed catalyst powder (30 wt.% metal on carbon (Vulcan XC-72), a Nafion solution (5 wt.% in alcohols/water, Aldrich) and a methanol/water solution. The mixture was treated with an ultrasonic probe (Misonic 3000 sonicator, pulse mode) for 1 h. The ink was then sprayed on CFP using an auto-spray (nozzle-XY table) system. The resulting GDE and the membrane were then hot-pressed at 80 kg cm^{-2} and 140 °C for 4 min. The catalyst metal loading was 2 mg cm^{-2} for both the anode and the cathode, while the Nafion composition in the catalyst layer was 20 wt.%. Both commercial $Pt_{67}Ru_{33}/C$ (1:1) (Johnson Matthey Inc. HISPEC5000) and $Pt_{83}Sn_{17}/C$ (3:1) (E-tek) were used in the fuel cell test as reference binary compositions. All fuel cell tests were conducted at 90 °C with oxygen supplied to the cathode at a flow rate of 300 ml min^{-1} and atmospheric pressure. The anode was supplied with a preheated 1 M solution of ethanol (in DI water) at a flow rate of 2.0 ml min^{-1}.

3. Results and discussion

3.1. Physicochemical characterization

Table 1 shows the comparison between nominal and actual compositions of prepared catalysts. The relative composition of Pt
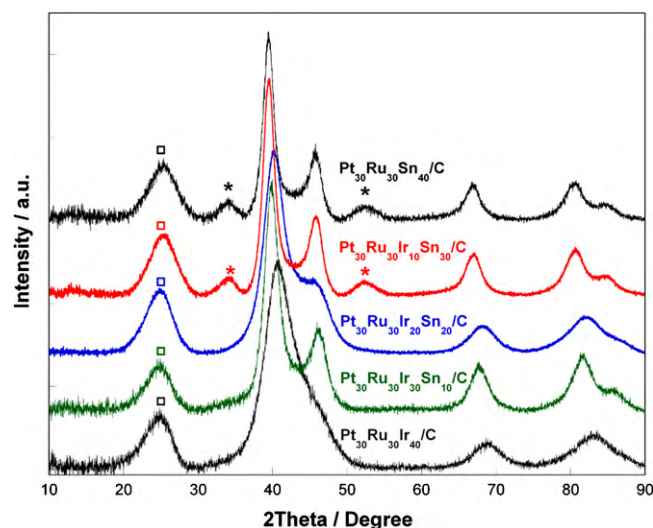
(at.%) remains unchanged in the quaternary catalysts, but enrichment and depletion were observed with the ternary catalysts $Pt_{30}Ru_{30}Sn_{40}/C$ and $Pt_{30}Ru_{30}Ir_{40}/C$, respectively. The increase in Sn content clearly resulted in a serious Ru depletion in the catalyst compared to the nominal composition. Sine et al. [33] observed a similar Ru depletion on the surface of a PtRuSn ternary catalyst based on an XPS study, which was explained as Ru being repelled from the catalyst surface by Sn. For the commercial catalyst, PtRu HISPEC5000, a good agreement is shown between the actual and nominal composition. Fig. 2 shows the XRD patterns of the prepared carbon-supported quaternary $Pt_{30}Ru_{30}Ir_{40-x}Sn_x/C$ electrocatalysts with 30% metal loading. In all of the patterns, the main characteristics of the face-centered cubic lattice (fcc) of Pt-based phase(s) were observed. The substitution of Ir with Sn clearly shifts the diffraction lines toward lower 2θ values, indicating an expansion of the Pt-based phase(s). Two diffraction peaks corresponding to a SnO_2 phase in both Sn-rich compositions were apparent at 34.01° and 52.27° for $Pt_{30}Ru_{30}Ir_{10}Sn_{30}/C$ and at 33.99° and 52.21° for $Pt_{30}Ru_{30}Sn_{40}/C$. No peak corresponding to SnO_2 was detected in $Pt_{30}Ru_{30}Ir_{30}Sn_{10}/C$ and $Pt_{30}Ru_{30}Ir_{20}Sn_{20}/C$, which is likely due to phase saturation toward Sn under the present preparation conditions. The composition $Pt_{30}Ru_{30}Ir_{40}/C$ shows unresolved main peaks in the 2θ range of 35–50°, which could be due to a stronger overlap of diffraction peaks of different possible phases as well as to nano-sized crystallites. A high resolution TEM image of $Pt_{30}Ru_{30}Ir_{10}Sn_{30}/C$ is shown in Fig. 3a, illustrating the microstructure of the quaternary carbon-supported catalyst. It is seen that particles of a few nanometres are intimately bound to form larger agglomerates. Some well-defined fringe fingerprints were used to measure the interplanar spacing (d spacing) by line-profile, as shown in Fig. 3b. The d spacing 2.27–2.29 Å and 1.97 Å were attributed, respectively, to (1 1 1) and (2 0 0) planes of an expanded Pt-based phase. The corresponding lattice parameter was calculated to be in the range 3.932–3.966 Å. The presence of d spacing 2.07–2.11 Å was attributed to (1 0 1) plane of a hexagonal Ru-based phase, which was not apparent in the XRD pattern. The d spacing of 2.38 Å was also observed, which could be attributed to either (2 0 0) plane of SnO_2 or to an expanded (1 0 0) d spacing of a Ru-based phase. Although the XRD pattern showed peaks corresponding to a SnO_2 phase, the d spacing corresponding to these peaks could not be detected in the HRTEM image.
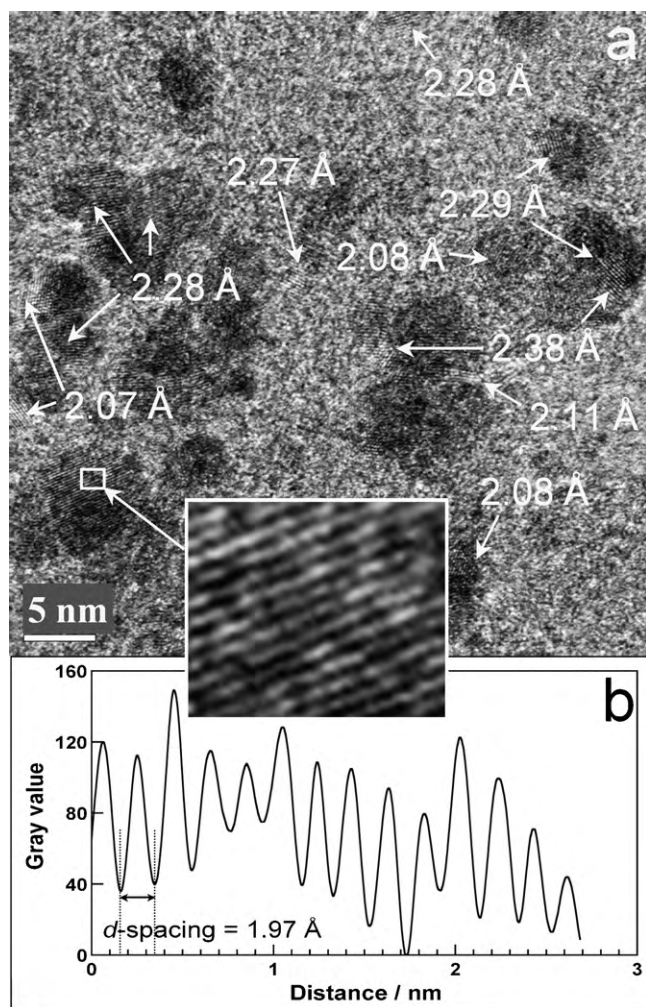
Fig. 3. (a) HRTEM micrograph (1050k×) of $Pt_{30}Ru_{30}Ir_{10}Sn_{30}/C$ and (b) profile analysis of fringe fingerprints for d spacing evaluation.

Fig. 4. Example of XRD whole pattern decomposition using Pawley refinement method.

The HRTEM image suggested not only the presence of a Pt-based phase, as is apparent from the XRD patterns, but also the presence of a Ru-based phase. It is also seen that some agglomerates include intimately joint particles with d spacing from both phases. Based on these observations, an attempt was made to refine the XRD patterns to derive a more reliable lattice and crystallites size parameters using the Pawley method [34]. TOPAS software from Bruker AXS was used for the whole pattern decomposition. Peak

positions were corrected separately for all patterns using LaB_6 as an internal standard. The LaB_6 standard was also used to correct for the instrument contribution to the peak width for estimation of the crystallite sizes. The lattice parameter and the average crystallite sizes were estimated using whole pattern fitting with the most probable space groups as follows (as deduced from XRD patterns and the HRTEM image): $Fm-3m$ representing cubic Pt and/or Ir-like phases and $P63/mmc$ representing hexagonal Ru-like structures. When SnO_2 is present, the fitting included the space group $P42/mnm$ corresponding to a tetragonal SnO_2 phase. The instrumental parameters were obtained by fitting the XRD pattern of the LaB_6 standard. Fig. 4 shows an example of XRD pattern fitting. The quality of the fit was assessed both visually and via calculated figures of merit. From this fitting, a Pt-based structure seems to be the main phase. Table 2 presents the fitted lattice parameter and crystallite sizes for each phase in the studied catalyst compositions. It is clear that the substitution of Ir with Sn resulted in an

Table 2

Lattice parameters, crystallite sizes by Pawley refinement of XRD patterns and BET specific surface area of $Pt_{30}Ru_{30}Ir_{40-x}Sn_x/C$.

Electrocatalyst	Nominal composition (wt.%)	Possible phases S.G.[a]	Lattice parameters (Å)	Crystallites size (nm)	R_{wp}/R_{exp}[b]	BET surface (m² g⁻¹)
PtRuIrSn/C	30:30:40:0	$Fm-3m$	$a = 3.877$	2.6	1.04	387.4
		$P63/mmc$	$a = 2.694, c = 4.344$	1.6		
	30:30:30:10	$Fm-3m$	$a = 3.909$	4.2	1.64	214.4
		$P63/mmc$	$a = 2.662, c = 4.251$	3.6		
	30:30:20:20	$Fm-3m$	$a = 3.895$	3.0	1.48	–
		$P63/mmc$	$a = 2.630, c = 4.242$	2.4		
	30:30:10:30	$Fm-3m$	$a = 3.945$	5.3	1.28	174.9
		$P63/mmc$	$a = 2.591, c = 4.228$	3.0		
		$P42/mnm$	$a = 4.688, c = 3.192$	2.1		
	30:30:0:40	$Fm-3m$	$a = 3.953$	5.5	1.04	174.6
		$P63/mmc$	$a = 2.600, c = 4.221$	3.3		
		$P42/mnm$	$a = 4.694, c = 3.186$	2.1		

[a] Space group used in whole pattern fitting: $Fm-3m$ used for cubic Pt, Ir-based phase, $P63/mmc$ for hexagonal Ru-based phase and $P42/mnm$ for tetragonal SnO_2.
[b] Goodness of fit (GOF).

increase of the lattice parameter of the main Pt-based phase from 3.877 to 3.953 Å, which was expected because the radius of Sn is larger than Ir. For $Pt_{30}Ru_{30}Ir_{40}$/C, the lattice parameter of 3.877 Å is more likely to correspond to an expanded lattice of an Ir-based phase (3.840 Å for pure Ir) rather than a compressed lattice of a Pt-based phase (3.923 Å for pure Pt). A higher content of Sn also led to larger crystallite sizes, which increased for the main phase from an average of 2.6–5.5 nm. This result is in a good agreement with BET measurements (Table 2), which show a surface decrease with the substitution of Ir with Sn from 387.4 to 174.6 $m^2 g^{-1}$. The lattice parameters of the Ru-based phase seem to decrease with Sn substitution. However, this trend is difficult to confirm because the peaks corresponding to the hexagonal Ru-based phase are not clearly distinct in the diffraction pattern. For the SnO_2 phases, the lattice parameters and average crystallite size showed similar values in both $Pt_{30}Ru_{30}Ir_{10}Sn_{30}$/C and $Pt_{30}Ru_{30}Sn_{40}$/C. The fitting showed that SnO_2 exhibit consistent average crystallite sizes of 2.1 nm. It can be deduced from the HRTEM and XRD results that the prepared $Pt_{30}Ru_{30}Ir_{40-x}Sn_x$/C catalysts produced via the boro-hydride reduction method exist mainly as Pt-based alloy as well as a small proportion of Ru-based alloy. It is worth noting that the main Pt-based phase can exist both as solid solution alloy and/or as separate phases having similar cubic fcc structure. Additionally, for a higher content of Sn, SnO_2 is produced. The HRTEM image of $Pt_{30}Ru_{30}Ir_{10}Sn_{30}$/C established the occurrence of a lattice parameter distribution within the same composition, as shown for the Pt (1 1 1) as well as Ru (1 0 1) planes. This outcome occurs mainly because the catalyst particles are growing in the reduction process from adsorbed metal ions on the carbon support and thus are dependent on the adsorption sites, metal ion complexes and their ratio at a particular carbon site. BET surface analysis confirms the increase of particle sizes with increasing Sn content as was deduced from the XRD analysis.

Fig. 5a presents a typical TEM image showing an overview of the catalysts dispersion on carbon XC-72 obtained by the borohydride reduction method. Based on more than 100 counts, a wide distribution of particle sizes was obtained, as shown in the histogram of Fig. 5b, with an average of 4.9 nm and a standard deviation (STDV) of 2.5 nm. Larger particles (>10 nm) were also present but in a smaller proportion. This TEM-obtained particle size distribution is in the same range as the average crystallite sizes determined by XRD.

3.2. Ethanol oxidation activity

The electrocatalytic activity of supported $Pt_{30}Ru_{30}Ir_{40-x}Sn_x$/C electrocatalysts (30 wt.% metal load) was evaluated for EOR for different Ir and Sn contents. Fig. 6a shows the average polarization curves obtained in 1 M EtOH + 0.5 M H_2SO_4 by linear sweep voltammetry (without electrode rotation) at a scan rate of 1 mV/s in the potential range of 0–0.6 V vs. SHE. The performance was evaluated with respect to the same Pt loading of 27 $\mu g\,cm^{-2}$ in each electrode based on the actual composition obtained by EDX. The catalyst compositions $Pt_{30}Ru_{30}Ir_{40}$/C and $Pt_{30}Ru_{30}Sn_{40}$/C exhibited the lowest activity for ethanol oxidation, particularly at potentials above 0.45 V vs. SHE. Below 0.45 V, their activity is rather similar to the commercial $Pt_{67}Ru_{33}$/C catalyst. A higher current density of ethanol electro-oxidation was obtained with the compositions $Pt_{30}Ru_{30}Ir_{10}Sn_{30}$/C, $Pt_{30}Ru_{30}Ir_{20}Sn_{20}$/C and $Pt_{30}Ru_{30}Ir_{30}Sn_{10}$/C; however, the activity of the latter is lower than $Pt_{67}Ru_{33}$/C above 0.45 V. The substitution of more than 50% (wt.%) of Ir content with Sn seems to improve the performance up to 0.5 V. At 0.6 V, the activity of these active catalysts turns out to be similar to commercial $Pt_{67}Ru_{33}$/C. The catalysts $Pt_{30}Ru_{30}Ir_{10}Sn_{30}$/C and $Pt_{30}Ru_{30}Ir_{20}Sn_{20}$/C demonstrated a higher activity compared to commercial $Pt_{67}Ru_{33}$/C, but only in the potential region 0.2–0.5 V.
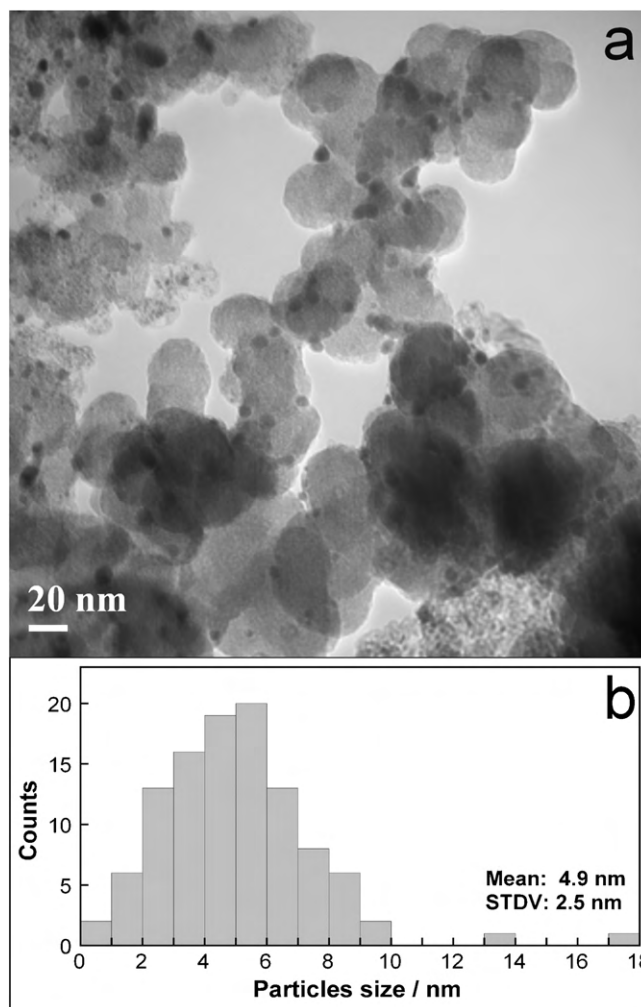

Fig. 5. (a) Typical TEM micrograph (400k×) and (b) histogram of particle size distribution of $Pt_{30}Ru_{30}Ir_{40-x}Sn_x$/C electrocatalysts prepared by borohydride method.

Fig. 6b shows the average polarization curve and experimental deviation for $Pt_{30}Ru_{30}Ir_{10}Sn_{30}$/C and $Pt_{67}Ru_{33}$/C. The polarization curves were repeated at least nine times for a given composition (three different electrodes prepared from three different catalyst batches). Fig. 6b clearly shows the improvement of the performance compared to commercial $Pt_{67}Ru_{33}$/C in the potential region 0.2–0.5 V. Generally, it was observed that the polarization curves (not shown here) of catalysts containing Sn exhibit higher deviations in the potential region of 0.1–0.4 V, while $Pt_{30}Ru_{30}Ir_{40}$/C and commercial $Pt_{67}Ru_{33}$/C exhibit higher deviations at potentials higher than 0.4 V. Besides the factual variations in catalyst preparation (composition and structure) and electrode preparation and pre-treatment, this behavior may indirectly relate to the sensitivity of the ethanol electro-oxidation mechanism to Sn content in low potential region <0.4 V and is probably more sensitive to Ru content at higher potentials. It worth noting that in this studied potential region, only dehydrogenation or partial oxidation of ethanol may take place with such types of materials [7].

3.3. DEFC testing

Fuel cell performance for a direct ethanol fuel cell was evaluated on MEAs made with catalysts of nominal compositions as follows: $Pt_{30}Ru_{30}Ir_{10}Sn_{30}$/C; $Pt_{30}Ru_{30}Ir_{40}$/C; $Pt_{30}Ru_{30}Sn_{40}$/C; and commercial $Pt_{67}Ru_{33}$/C and $Pt_{83}Sn_{17}$/C (E-tek). We based our choice of these compositions on the most performing catalyst with the lowest pre-
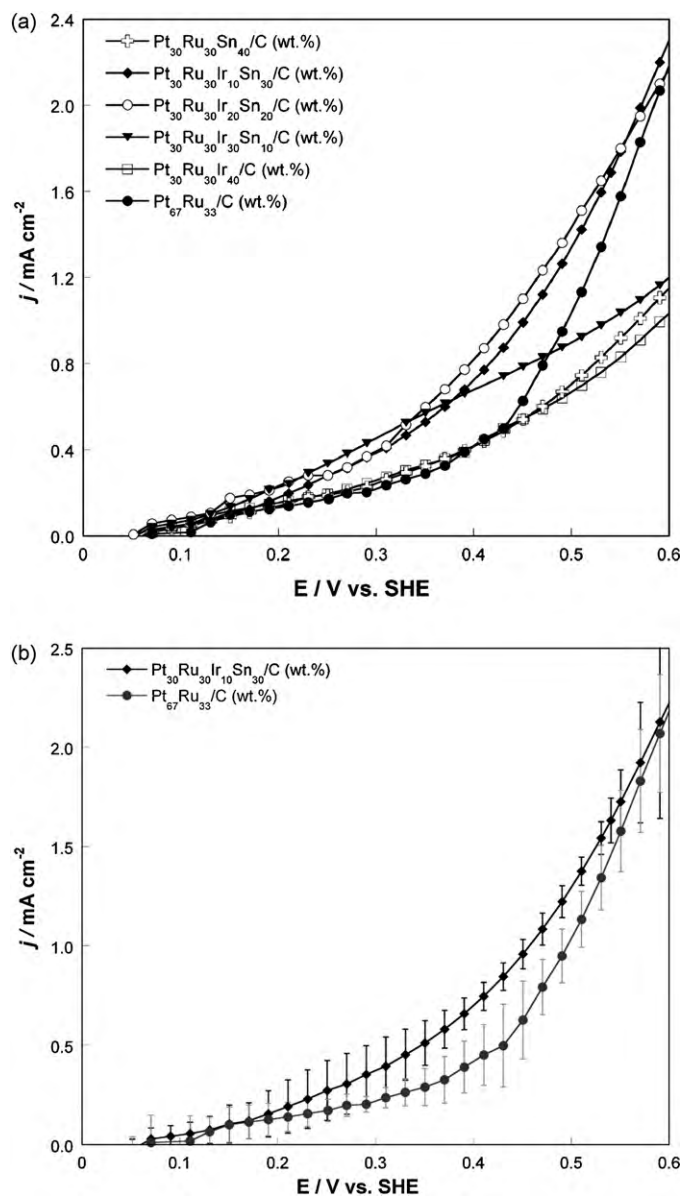
Fig. 6. (a) LSV polarization curves of $Pt_{30}Ru_{30}Ir_{40-x}Sn_x/C$ and $Pt_{67}Ru_{33}/C$ (1:1) (Johnson Matthey Inc.) recorded in 1 M EtOH + 0.5 M H_2SO_4 at 20 °C with a scan rate of 1 mV s^{-1}. (b) Example of fluctuations in LSV curves obtained with different catalyst and electrode preparation batches.

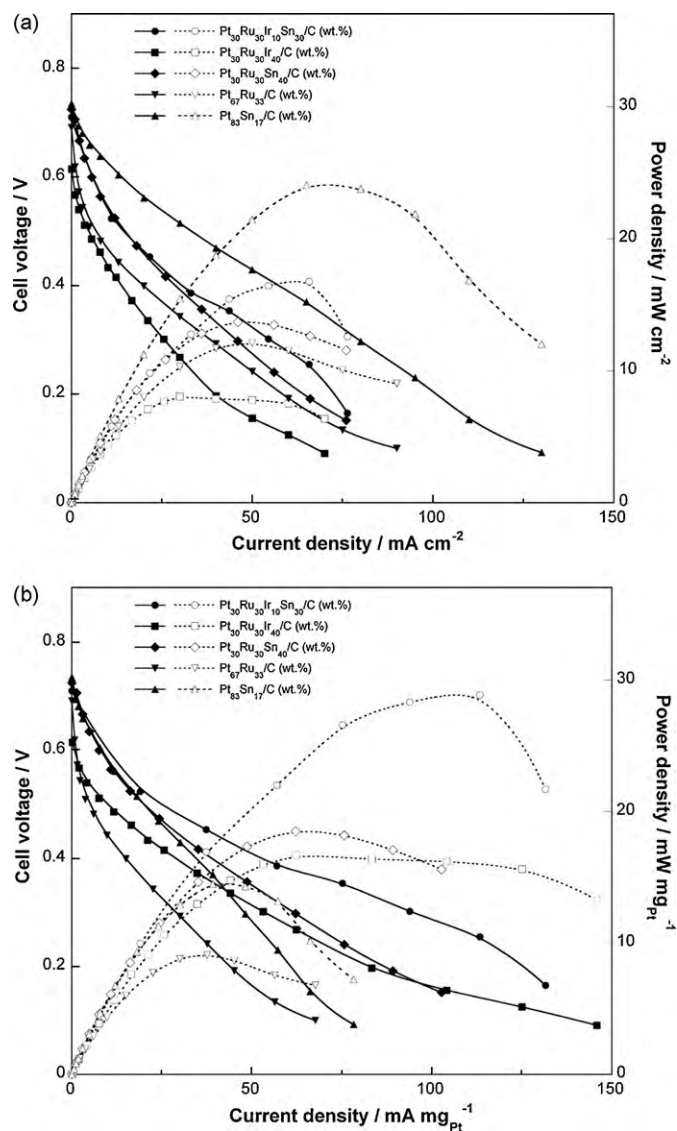**Fig. 7.** Beginning of life (BoL) DEFC performance's characteristics of $Pt_{30}Ru_{30}Ir_{40-x}Sn_x/C$ (x = 0, 30, 40), commercial $Pt_{67}Ru_{33}/C$ (1:1) (Johnson Matthey Inc.) and $Pt_{83}Sn_{17}/C$ (3:1) (E-tek). Current normalized to (a) surface area of the MEA and (b) Pt loading at the anode.

cious metals content for the quaternary catalyst, which is compared to the two studied limit compositions representing ternary catalysts and two binary commercial catalysts. Prior to polarization curve measurement, the break-in of the MEA was performed by setting a constant cell voltage of 0.2 V for 2–4 h until the current was stable. All polarization measurements were conducted in galvanostatic mode.

Fig. 7a shows the beginning of life (BoL) performance normalized with respect to the geometric surface area of the MEA. The composition $Pt_{30}Ru_{30}Ir_{10}Sn_{30}/C$ (1:1.5:0.5:2) showed a better maximum power density compared to commercial $Pt_{67}Ru_{33}/C$, which indicates an improved activity with a lower platinum loading. However, the performance is still lower than commercial $Pt_{83}Sn_{17}/C$. When the performance is reported with respect to Pt loading (EDX) at the anode as illustrated in Fig. 7b, the composition $Pt_{30}Ru_{30}Ir_{10}Sn_{30}/C$ (1:1.5:0.5:2) showed the best performance with a maximum specific power density of 29 mW mg$_{Pt}^{-1}$ followed by $Pt_{30}Ru_{30}Sn_{40}/C$ (1:0.8:2) with 19 mW mg$_{Pt}^{-1}$. Both composi-

tions showed similar kinetic behavior as commercial $Pt_{83}Sn_{17}/C$. The specific power density obtained with $Pt_{30}Ru_{30}Sn_{40}/C$ (1:0.8:2) is consistent with the results obtained by Zhou et al. [14] for PtRuSn/C (1:1:1), but the authors did not specify the cathode operating conditions for oxygen pressure and flow rate. Commercial $Pt_{67}Ru_{33}/C$ showed the lowest power density of 9 mW mg$_{Pt}^{-1}$, while the composition $Pt_{30}Ru_{30}Ir_{40}/C$ and commercial $Pt_{83}Sn_{17}/C$ showed specific power densities around 17 and 15 mW mg$_{Pt}^{-1}$, respectively. However, $Pt_{30}Ru_{30}Ir_{40}/C$ exhibited this power density over an extended region of current density. Both $Pt_{30}Ru_{30}Ir_{40}/C$ and commercial $Pt_{67}Ru_{33}/C$ showed a lower performance in the kinetic region of the polarization curve. Except for the compositions $Pt_{30}Ru_{30}Ir_{10}Sn_{30}/C$ vs. $Pt_{67}Ru_{33}/C$, the behavior exhibited in the kinetic region of BoL polarization curves of the other catalysts does not agree well with the trend observed in LSV polarization curves. This discrepancy seems to be due to the overall experimental condition differences between half-cell and fuel cell testing.

The presence of Sn in the quaternary $Pt_{30}Ru_{30}Ir_{10}Sn_{30}/C$ and ternary $Pt_{30}Ru_{30}Sn_{40}/C$ catalyst clearly increased the overall fuel
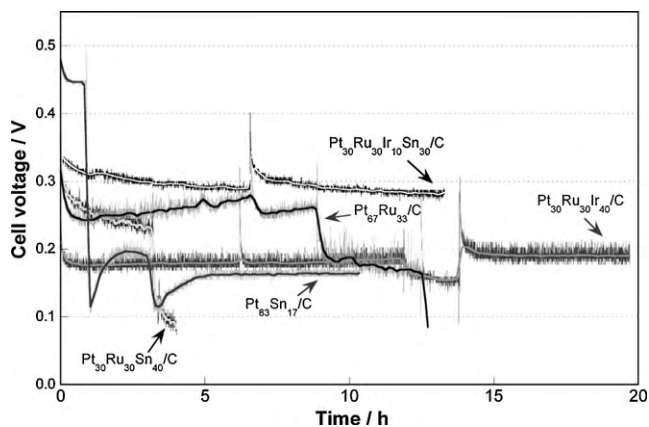
Fig. 8. DEFC performance's durability test at $40\,mA\,cm^{-2}$ of $Pt_{30}Ru_{30}Ir_{40-x}Sn_x/C$ ($x = 0$, 30, 40), commercial $Pt_{67}Ru_{33}/C$ (1:1) (Johnson Matthey Inc.) and $Pt_{83}Sn_{17}/C$ (3:1) (E-tek).

cell performance compared to $Pt_{30}Ru_{30}Ir_{40}/C$ and $Pt_{67}Ru_{33}/C$, respectively. Moreover, BET and XRD results showed that catalysts with high contents of Sn exhibit lower specific surface area and larger crystallite sizes, suggesting that the performance of $Pt_{30}Ru_{30}Ir_{10}Sn_{30}/C$ and ternary $Pt_{30}Ru_{30}Sn_{40}/C$ could be improved further by increasing the specific surface area. The effect of Ir in $Pt_{30}Ru_{30}Ir_{40}/C$ (1:2.7:1.8) compared to $Pt_{67}Ru_{33}/C$ (1:1) is not only important in terms of maximum specific power density but also in terms of operation at higher current densities. This result clearly shows both the activating and stabilizing effect of Ir. Liang et al. [21] attributed the positive effect of Ir in their anode PtRuIr/C catalyst (1:1:1) (40 wt.% metal loading) to the interaction between IrO_2 and RuO_2 toward the oxidation of CO-like species. Interestingly, their sample, 30% (PtRuIr)/C (1:1.9:1.4) with twice the Ru content showed the lowest performance.

3.4. DEFC durability test

The majority of published studies investigated the durability performance on binary and ternary Pt-based catalysts for DEFC using chronoamperometry experiments at 400 mV for periods between 15 and 120 min. In the present work, the durability study was carried out in the fuel cell immediately after recording the BoL polarization curve. Fig. 8 presents the cell voltage at a constant current density of $40\,mA\,cm^{-2}$ illustrating the durability of prepared catalysts. The spike in the cell voltage indicates the restart after 6–7 h of continuous cell operation. When severe performance degradation was observed, the measurement was restarted again with the same MEA. A marked initial decay of the cell voltage was observed with $Pt_{30}Ru_{30}Sn_{40}/C$ and commercial $Pt_{67}Ru_{33}/C$. The latter showed some intermittent performance gain, but irreversible performance loss was observed over 12 h. For $Pt_{30}Ru_{30}Sn_{40}/C$, irreversible performance loss was observed earlier after just 4 h. For commercial $Pt_{83}Sn_{17}/C$, consistent performance degradation was observed after testing times as short as 1 or 2 h. Besides the poisoning of the catalyst's active sites by the reaction intermediates and products, the stability of these catalysts needs to be further investigated. Conversely, both catalysts $Pt_{30}Ru_{30}Ir_{10}Sn_{30}/C$ and $Pt_{30}Ru_{30}Ir_{40}/C$ containing Ir showed stable performance for more than 14 h. These two compositions also demonstrate a recovery to the initial performance after the fuel cell was restarted, indicating a reversible degradation mechanism. According to these results, Sn clearly promoted the kinetics of ethanol oxidation and increased the initial cell performance in $Pt_{30}Ru_{30}Sn_{40}/C$ and $Pt_{83}Sn_{17}/C$ compared to $Pt_{67}Ru_{33}/C$ catalyst (Fig. 7b), but the long-term performance stability of the catalyst is deficient. Ir increased
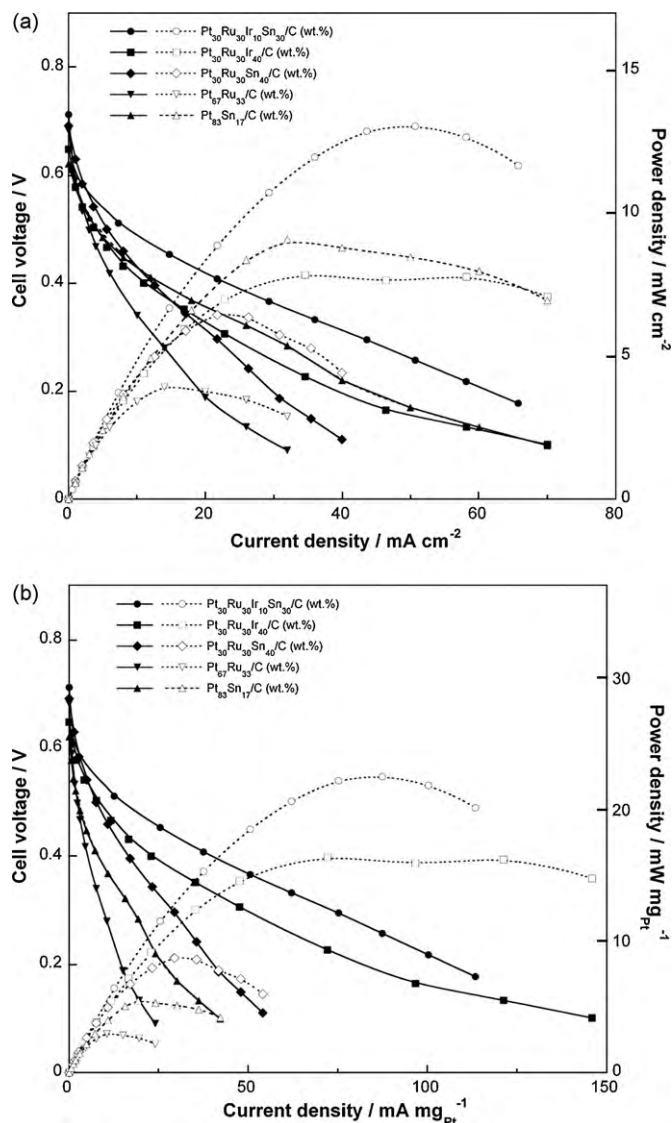

Fig. 9. Post-durability DEFC performance's characteristics of $Pt_{30}Ru_{30}Ir_{40-x}Sn_x/C$ ($x = 0$, 30, 40), commercial $Pt_{67}Ru_{33}/C$ (1:1) (Johnson Matthey Inc.) and $Pt_{83}Sn_{17}/C$ (3:1) (E-tek). Current normalized to (a) surface area of the MEA and (b) Pt loading at the anode.

the long-term performance stability with a minor performance decrease.

This durability study showed that $Pt_{30}Ru_{30}Ir_{10}Sn_{30}/C$ not only exhibited the best DEFC performance but also excellent long-term performance stability. These findings are well-illustrated in Fig. 9a and b showing polarization curves recorded after the durability test normalized to the MEA surface area and platinum loading, respectively. The maximum power density of commercial $Pt_{83}Sn_{17}/C$ was then lower than $Pt_{30}Ru_{30}Ir_{10}Sn_{30}/C$ in both cases. The maximum specific power density of $Pt_{30}Ru_{30}Ir_{10}Sn_{30}/C$ showed a 20% loss over 14 h of continuous operation, and almost no loss was observed with $Pt_{30}Ru_{30}Ir_{40}/C$ over 20 h. Conversely, over a shorter operation time, $Pt_{30}Ru_{30}Sn_{40}/C$, $Pt_{83}Sn_{17}/C$ and $Pt_{67}Ru_{33}/C$ showed a maximum power density loss of 52, 64 and 67%, respectively. At this stage, it is difficult to draw meaningful conclusions around this behavior because more post-durability investigations are needed regarding the catalyst composition, reaction products analysis, MEA diagnostics and more. However, it is believed that the excellent corrosion resistance and mechanical properties of Ir are shown in $Pt_{30}Ru_{30}Ir_{10}Sn_{30}/C$ and $Pt_{30}Ru_{30}Ir_{40}/C$ performances despite the

fuel cell being operated in relatively harsh conditions of temperature. In addition, it is also believed that Ir reduces the poisoning of active sites with EOR intermediates and products. In the absence of Ir, the performance degradation of $Pt_{30}Ru_{30}Sn_{40}/C$, $Pt_{83}Sn_{17}/C$ and $Pt_{67}Ru_{33}/C$ catalysts could be due to poisoning, but it could also be due to Ru and Sn dissolution and depletion during fuel cell operation. This dissolution could even be the main factor in such performance degradation, which needs to be further investigated.

4. Conclusion

The investigation of a series of quaternary electrocatalysts, $Pt_{30}Ru_{30}Ir_{40-x}Sn_x/C$ (wt.%), for ethanol electro-oxidation reactions (EOR) demonstrated that these catalysts crystallize mainly as fcc Pt-based phases. HRTEM revealed the presence of a hexagonal Ru-based phase but most likely in a smaller proportion. The increase in Sn content increased the crystallite sizes and reduced the specific surface area, as revealed by BET results. A very good performance and an excellent long-term stability were achieved with the composition $Pt_{30}Ru_{30}Ir_{10}Sn_{30}/C$ compared to commercial $Pt_{67}Ru_{33}/C$ (1:1) (HISPEC 5000) and $Pt_{83}Sn_{17}/C$ (3:1) (E-tek). This low Pt content catalyst (30 wt.% or 20 mol.% of Pt) exhibited both the promoting effect of Ru and Sn in the working potential range and the stabilizing effect of Ir. However, a post-durability study is required to understand this behavior and correlate the performance to the catalyst properties.

Acknowledgments

References

[1] F. Vigier, C. Coutanceau, F. Hahn, E.M. Belgsir, C. Lamy, J. Electroanal. Chem. 563 (2004) 81.
[2] E. Antolini, J. Power Sources 170 (2007) 1.
[3] G.A. Camara, R.B. de Lima, T. Iwasita, J. Electroanal. Chem. 585 (2005) 128.
[4] F. Colmati, E. Antolini, E.R. Gonzalez, J. Power Sources 157 (2006) 98.
[5] L. Colmenares, H. Wang, Z. Jusys, L. Jiang, S. Yan, G.Q. Sun, R.J. Behm, Electrochim. Acta 52 (2006) 221.
[6] L. Jiang, G. Sun, S. Sun, J. Liu, S. Tang, H. Li, B. Zhou, Q. Xin, Electrochim. Acta 50 (2005) 5384.
[7] H. Li, G. Sun, L. Cao, L. Jiang, Q. Xin, Electrochim. Acta 52 (2007) 6622.
[8] D.R. Lycke, E.L. Gyenge, Electrochim. Acta 52 (2007) 4287.
[9] S. Song, P. Tsiakaras, Appl. Catal. B: Environ. 63 (2006) 187.
[10] H. Wang, Z. Jusys, R.J. Behm, J. Power Sources 154 (2006) 351.
[11] W.J. Zhou, B. Zhou, W.Z. Li, Z.H. Zhou, S.Q. Song, G.Q. Sun, Q. Xin, S. Douvartzides, M. Goula, P. Tsiakaras, J. Power Sources 126 (2004) 16.
[12] M. Zhu, G. Sun, H. Li, L. Cao, Q. Xin, Chinese J. Catal. 29 (2008) 765.
[13] E. Antolini, F. Colmati, E.R. Gonzalez, Electrochem. Commun. 9 (2007) 398.
[14] W.J. Zhou, W.Z. Li, S.Q. Song, Z.H. Zhou, L.H. Jiang, G.Q. Sun, Q. Xin, K. Poulianitis, S. Kontou, P. Tsiakaras, J. Power Sources 131 (2004) 217.
[15] S. Rousseau, C. Coutanceau, C. Lamy, J.-M. Léger, J. Power Sources 158 (2006) 18.
[16] F. Vigier, C. Coutanceau, A. Perrard, E.M. Belgsir, C. Lamy, J. Appl. Electrochem. 34 (2004) 439.
[17] C. Lamy, S. Rousseau, E.M. Belgsir, C. Coutanceau, J.-M. Léger, Electrochim. Acta 49 (2004) 3901.
[18] W. Zhou, Z. Zhou, S. Song, W. Li, G. Sun, P. Tsiakaras, Q. Xin, Appl. Catal. B 46 (2003) 273.
[19] L. Cao, G. Sun, H. Li, Q. Xin, Electrochem. Commun. 9 (2007) 2541.
[20] P. Sivakumar, V. Tricoli, Electrochem. Solid State Lett. 9 (2006) A167–A170.
[21] Y. Liang, H. Zhang, H. Zhong, X. Zhu, Z. Tian, D. Xu, B. Yi, J. Catal. 238 (2006) 468.
[22] N.R. de Tacconi, R.O. Lezna, B. Beden, F. Hahn, C. Lamy, J. Electroanal. Chem. 379 (1994) 329.
[23] M.L. Calegaro, H.B. Suffredini, S.A.S. Machado, L.A. Avaca, J. Power Sources 156 (2006) 300.
[24] A. Chen, D.J. La Russa, B. Miller, Langmuir 20 (2004) 9695.
[25] Y. Morimoto, Res. Dev. Rev. Toyota CRDL 33 (1998) 43.
[26] T. Ioroi, N. Kitazawa, K. Yasuda, Y. Yamamoto, H. Takenaka, J. Electrochem. Soc. 147 (2000) 2018.
[27] T. Ioroi, K. Yasuda, J. Electrochem. Soc. 152 (2005) A1917–A1924.
[28] J. Ribeiro, D.M. dos Anjos, K.B. Kokoh, C. Coutanceau, J.-M. Léger, P. Olivi, A.R. de Andrade, G. Tremiliosi-Filho, Electrochim. Acta 52 (2007) 6997.
[29] K.L. Ley, R. Liu, C. Pu, Q. Fan, N. Leyarovska, C. Segre, E.S. Smotkin, J. Electrochem. Soc. 144 (1997) 1543.
[30] B. Gurau, R. Viswanathan, R. Liu, T.J. Lafrenz, K.L. Ley, E.S. Smotkin, E. Reddington, A. Sapienza, B.C. Chan, T.E. Mallouk, S. Sarangapani, J. Phys. Chem. B 102 (1998) 9997.
[31] A.S. Arico, Z. Poltarzewski, H. Kim, A. Morana, N. Giordano, V. Antonucci, J. Power Sources 55 (1995) 159.
[32] K. Fatih, D.P. Wilkinson, F. Moraw, A. Ilicic, F. Girard, Electrochem. Solid State Lett. 11 (2008) B11–B15.
[33] G. Sine, D. Smida, M. Limat, G. Foti, C. Comninellis, J. Electrochem. Soc. 154 (2007) B170–B174.
[34] G.S. Pawley, J. Appl. Cryst. 14 (1981) 357.